AIAA JOURNAL
Vol. 48, No. 12, December 2010

# Extending Weighted Compact Nonlinear Schemes to Complex Grids with Characteristic-Based Interface Conditions

Xiaogang Deng,* Meiliang Mao,† Guohua Tu,‡ Yifeng Zhang,§ and Hanxin Zhang¶
*State Key Laboratory of Aerodynamics, China Aerodynamics Research and Development Center, 621000 Mianyang, People's Republic of China*

DOI: 10.2514/1.J050285

**There are still some challenges, such as grid quality, numerical stability, and boundary schemes, in the practical application of high-order finite difference schemes for complex configurations. This study presents some improved strategies that indicate potential engineering applications of high-order schemes. The formally fifth-order weighted compact nonlinear scheme developed by the authors is implemented on point-matched multiblock structured grids, which are generated over complex configurations to ensure the grid quality of each component block. The information transmission between neighboring blocks is carried out by new characteristic-based interface conditions that directly exchange the spatial derivatives on each side of an interface by means of a characteristic-based projection to keep the high-order accuracy and high resolution of a spatial difference scheme. The high-order scheme combined with the interface conditions is shown to be asymptotically stable. The engineering-oriented applications of the high-order strategy are demonstrated by solving several two- and three-dimensional problems with complex grid systems.**

## Nomenclature

| | | |
|---|---|---|
| $a$ | = | speed of sound |
| $c$ | = | chord length |
| $E$ | = | nondimensional total energy |
| $F, G, H$ | = | fluxes in Cartesian coordinates |
| $\hat{F}, \hat{G}, \hat{H}$ | = | fluxes in curvilinear coordinates |
| $h$ | = | grid size |
| $J$ | = | Jacobian of coordinate transformation, $\partial(\xi, \eta, \zeta)/\partial(x, y, z)$ |
| $L$ | = | left eigenvector |
| $Ma$ | = | Mach number |
| $P_{QV_C}$ | = | transformation matrix, $\partial Q/\partial V_C$ |
| $p$ | = | nondimensional pressure |
| $Q$ | = | conservative variable vector |
| $q$ | = | heat transfer rate |
| $Re$ | = | Reynolds number |
| RHS | = | right-hand-side terms |
| $T$ | = | nondimensional temperature |
| $T_\infty$ | = | inflow temperature, K |
| $t$ | = | nondimensional time |
| $u, v, w$ | = | nondimensional velocity components |
| $V_C$ | = | characteristic variable vector |
| $x, y, z$ | = | Cartesian coordinates |
| $\alpha$ | = | angle of attack, deg |
| $\gamma$ | = | special heat ratio, 1.4 |
| $\lambda$ | = | eigenvalue |
| $\mu$ | = | nondimensional dynamic viscosity |
| $\xi, \eta, \zeta$ | = | curvilinear coordinates |
| $\xi_x, \hat{\xi}_x, \eta_x, \hat{\eta}_x$ | = | metrics (grid derivatives), $\hat{\xi}_x = J^{-1}\xi_x, \ldots$ |
| $\rho$ | = | nondimensional density |

*Subscripts*

| | | |
|---|---|---|
| $b$ | = | interface boundary between two blocks |
| $I$ | = | inviscid-related quantity |
| $L$ | = | left |
| $R$ | = | right |
| $V$ | = | viscous-related quantity |
| $w$ | = | wall |
| 0 | = | stagnation condition |
| $\infty$ | = | freestream condition |

Received 2 November 2009; revision received 27 April 2010; accepted for publication 22 June 2010. 

*Professor, Head of Laboratory, P.O. Box 211; xgdeng@skla.cardc.cn.
†Professor, P.O. Box 211; mlmao@skla.cardc.cn.
‡Assistant Researcher, P.O. Box 211; ghtu@skla.cardc.cn.
§Assistant Researcher, P.O. Box 211; yfzhang@skla.cardc.cn.
¶Academician of Chinese Academy of Sciences, National Laboratory for Computational Fluid Dynamics; hxzhang@skla.cardc.cn.

## I. Introduction

DESPITE the continuous progress in computational fluid dynamics (CFD) community, challenges still remain in the accurate numerical simulation of a broad spectrum of complex phenomena included in the direct-numerical simulation and large-eddy simulation of turbulence, aeroacoustics, fluid/structure interactions, and electromagnetics [1]. Although low-order schemes are widely used for engineering applications, they are insufficient for many viscosity-dominant domains, such as boundary-layer flows, vortex flows, shock/boundary-layer interactions, heat flux transfers, etc. An effective approach to overcome the obstacle of accurate numerical simulation is to employ high-order methods. A comprehensive review was given by Ekaterinaris [2] for high-order methods. Compact schemes with spectral-like resolution properties are more convenient to use than spectral and pseudospectral schemes and are easier to handle, especially when nontrivial geometries are involved [3]. However, central algorithms are intrinsically nondissipative and cannot prevent odd–even decoupling, which gives rise to high-frequency oscillations even in smooth regions. Reducing or removing such oscillations requires the introduction of dissipation terms. Upwind or upwind-based compact schemes with their dissipative properties are more stable than central schemes. Deng et al. [4] have proposed a type of one-parameter linear dissipative compact schemes, which was derived as to damp out the dispersive and parasite errors in the high-wave-number regions. Filters can also be applied to prevent numerical oscillations, such as the one proposed by Visbal and Gaitonde [5]. Some other methods resort to limiters, such as the compact-TVD schemes [6] and the characteristic-based shock-capturing compact scheme [7]. Nevertheless, in the transonic and supersonic flow regions when dealing with flows involving shock waves, one must use a numerical scheme that can both represent small scale structures with the minimum of

numerical dissipation and capture discontinuities with the robustness that is common to Godunov-type methods. To achieve these dual objectives, Deng et al. [4] have first developed compact nonlinear schemes with adaptive interpolations that can capture shock waves well [8]. Furthermore, weighted compact nonlinear schemes (WCNSs) have been derived by Deng and Zhang [9] and Deng [10]. The WCNS-E-5 [10], a typical explicit scheme of WCNS, has been successfully applied to a wide range of flow simulations so far to show its flexibility and robustness [11,12]. Nonomura et al. [13] showed that WCNS-E-5 is superior to the fifth-order weighted essentially nonoscillatory (WENO) scheme in freestream and vortex preservation on curvilinear grids. Recently, we proved that WCNSs can ensure the geometric conservation laws, while WENO schemes are difficult [12].

Traditionally, high-order schemes require high-quality grids. In practical flow computations with unsuitable structured grids, numerical instability is frequently observed around singular points with metric discontinuity [14]. However, it is difficult to generate a high-quality structured single-block grid system for a complex configuration. As one approach to solve complex flows, overset grid strategy for high-order compact schemes is used by Visbal and Gaitonde [5], Gaitonde and Visbal [15], Delfs [16], Sherer et al. [17,18], and other researchers. They employed point-to-point overlap grids or generalized overset grids with high-order Lagrange or B-spline interpolation methods. As interpolations in overset grids are generally necessary to allow the grid blocks to communicate with each other, numerical instability and loss of global accuracy will trouble the usage of high-order discretization formulas on overset grids. Furthermore, the grid configurations and numerical procedures for overset grid approach are generally complicated and not easy to implement for three-dimensional complex problems. Point-matched multiblock structured grids, or patched grids for more general means, are adopted alternative approaches for complex geometries. Multiblock structured grid technique makes it possible to run high-order finite difference schemes on each individual block, and the information transmission between neighboring blocks and the propagation throughout the flowfield can be realized by some kinds of interface conditions. Rai [19] made use of a flux interpolation to construct coupled conditions on midnode with Beam–Warming and Osher schemes. Lerat and Wu [20] adopted local flux construction to establish conservative and unconditionedly stable interface conditions. Kim and Lee [21] and Sumi et al. [14,22,23] employed characteristic interface conditions (CIC) or generalized characteristic interface conditions (GCIC). CIC/GCIC uses the inviscid characteristic relations straightforwardly derived from the flow transport equations and had been demonstrated excellent performance in practice [14].

However, because it is necessary to convert the governing equations to a characteristic form to compute the characteristic wave amplitude, the application of CIC or GCIC is not convenient. In this paper, we derive a new interface approach that directly exchanges the spatial derivatives (computed on each isolated block individually) on each side of an interface by means of a characteristic-based projection. Then it is no longer necessary to convert the governing equations to characteristic forms or to compute the characteristic wave-amplitude vector or other intermediate variables. The WCNS-E-5 [9–11] coupled with the new interface conditions is applied to solve some benchmark problems with complicated grid systems, such as the NLR7301 two-element airfoil, 30P-30N three-element airfoil (McDonnell Douglas 30P-30N landing configuration), and DLR-F6 (a wing-body civil aircraft configuration). The numerical results demonstrate that the present method can supply very smooth flowfields on complex multiblock structured grids.

The organization of this paper is as follows. Section II introduces the governing equations and the newly developed characteristic-based interface conditions. The high-order WCNS-E-5 scheme is introduced in Sec. III, and the asymptotic stability analysis of WCNS-E-5 with the interface conditions, together with a grid convergence test for the Burgers equation, is also given in Sec. III. In Sec. IV, the whole high-order difference strategy for complex structured grid systems is tested on several two- and three-dimensional benchmark problems. The conclusions are summarized in Sec. V.

## II. Governing Equations and Characteristic-Based Interface Conditions

### A. Governing Equations

The nondimensional strong conservative Navier–Stokes/Euler equations are selected and converted into curvilinear coordinates by introducing the transformation $(x, y, z) \rightarrow (\xi, \eta, \zeta)$ [17]:

$$\begin{cases} \frac{\partial \widehat{Q}}{\partial t} = \mathrm{RHS}_I + s \cdot \mathrm{RHS}_V \\ \mathrm{RHS}_I = -\frac{\partial \widehat{F}}{\partial \xi} - \frac{\partial \widehat{G}}{\partial \eta} - \frac{\partial \widehat{H}}{\partial \zeta} \\ \mathrm{RHS}_V = \frac{1}{Re}\left(\frac{\partial \widehat{F}_V}{\partial \xi} + \frac{\partial \widehat{G}_V}{\partial \eta} + \frac{\partial \widehat{H}_V}{\partial \zeta}\right) \end{cases} \tag{1}$$

where $s = 1$ for Navier–Stokes equations, and $s = 0$ for Euler equations. $\widehat{Q} = Q/J$, and $Q = [\rho, \rho u, \rho v, \rho w, \rho E]^T$ is the conservative variable vector. Here, $J = \partial(\xi, \eta, \zeta)/\partial(x, y, z)$ is the Jacobian of coordinate transformation.

### B. Characteristic-Based Interface Conditions

Characteristic theory has been used for the development of boundary conditions for many years. Barth [24] proposed a characteristic projection that can be conveniently applied to flow variables when constructing boundary fluxes. Thompson [25] and Poinsot and Lele [26] proposed characteristic boundary conditions for Euler and Navier–Stokes systems, respectively. Okong'o and Bellan [27] devised characteristic boundary conditions for multicomponent real-gas flows by following the local one-dimensional inviscid (LODI) relations of [26]. Kim and Lee [28] devised generalized characteristic boundary conditions in which the transverse and viscous terms are treated as source terms in addition to the LODI relations. The basic idea behind the characteristic boundary conditions of [26–28] is to split the convective terms in the boundary-normal direction into several waves with different characteristic velocities and then express unknown incoming waves as a function of known outgoing waves. These excellent boundary treatments are frequently applied to many areas, such as large-eddy simulations, direct numerical simulations, and computational aeroacoustics. Those studies enlightened us to devise the following characteristic-based interface conditions that satisfy the discrete governing equations.

To advance the characteristic analysis, the following transformation matrices are defined in terms of conservative variables $Q$ and characteristic variables $V_C$:

$$P_{QV_C} = \frac{\partial Q}{\partial V_C} \qquad \delta Q = \frac{\partial Q}{\partial V_C}\delta V_c \tag{2}$$

Hereafter, only the $\xi$ direction is taken into account without loss of generality. The $P_{QV_C}$ and $P^{-1}_{QV_C}$ can be found in many fluid studies, such as [28].

Equation (1) can be rearranged as

$$\frac{J^{-1}\partial Q}{\partial t} + J^{-1}\xi_x \frac{\partial F}{\partial \xi} + J^{-1}\xi_y \frac{\partial G}{\partial \xi} + J^{-1}\xi_z \frac{\partial H}{\partial \xi} = S_c \tag{3}$$

where

$$S_c = s \cdot \mathrm{RHS}_V - \left[F\frac{\partial J^{-1}\xi_x}{\partial \xi} + G\frac{\partial J^{-1}\xi_y}{\partial \xi} + H\frac{\partial J^{-1}\xi_z}{\partial \xi} + \frac{\partial J^{-1}\xi_t Q}{\partial \xi} + \frac{\partial \widehat{G}}{\partial \eta} + \frac{\partial \widehat{H}}{\partial \zeta}\right] \tag{4}$$

Let

$$A = \xi_x \frac{\partial F}{\partial Q} + \xi_y \frac{\partial G}{\partial Q} + \xi_z \frac{\partial H}{\partial Q} \tag{5}$$

Then $P_{QV_c}$ is the right characteristic matrix of $A$, and $P_{QV_c}^{-1} A P_{QV_c} = \Lambda$. Here,

$$\Lambda = \mathrm{diag}(\lambda_1, \lambda_2, \lambda_3, \lambda_4, \lambda_5) = \mathrm{diag}(\widehat{u}, \widehat{u}, \widehat{u}, \widehat{u} + \widehat{a}, \widehat{u} - \widehat{a})$$

$\widehat{u} = \xi_x u + \xi_y v + \xi_z w$, and $\widehat{a} = a\sqrt{\xi_x^2 + \xi_y^2 + \xi_z^2}$.

Let $\delta V_c = P_{QV_c}^{-1} \delta Q$; the last three terms on the left-hand side of Eq. (3) can be rewritten as

$$\begin{aligned} &J^{-1}\xi_x \frac{\partial F}{\partial \xi} + J^{-1}\xi_y \frac{\partial G}{\partial \xi} + J^{-1}\xi_z \frac{\partial H}{\partial \xi} = J^{-1} A \frac{\partial Q}{\partial \xi} = J^{-1} A \frac{\partial Q}{\partial V_c}\frac{\partial V_c}{\partial \xi} \\ &= J^{-1} A P_{QV_c} \frac{\partial V_c}{\partial \xi} = J^{-1} P_{QV_c} P_{QV_c}^{-1} A P_{QV_c} \frac{\partial V_c}{\partial \xi} = J^{-1} P_{QV_c} \Lambda \frac{\partial V_c}{\partial \xi} \end{aligned} \tag{6}$$

Inserting Eq. (6) into Eq. (3), we get

$$\frac{\partial Q}{\partial t} = JS_c - P_{QV_c} \Lambda \frac{\partial V_c}{\partial \xi} \tag{7}$$

Assume that the interface shown in Fig. 1 is along the $\xi$ direction with value $\xi_b$. Because the conservative variables and their time derivatives at the upstream limit and those at the downstream limit on the block interface are strictly matched, the following physical conditions are correct naturally:

$$\begin{aligned} &Q(t, \xi_b, \eta, \zeta)|_L = Q(t, \xi_b, \eta, \zeta)|_R, \\ &\left.\frac{\partial Q(t, \xi_b, \eta, \zeta)}{\partial t}\right|_L = \left.\frac{\partial Q(t, \xi_b, \eta, \zeta)}{\partial t}\right|_R \end{aligned} \tag{8}$$

Then

$$\left.\left(JS_c - P_{QV_c}\Lambda \frac{\partial V_c}{\partial \xi}\right)\right|_L = \left.\left(JS_c - P_{QV_c}\Lambda \frac{\partial V_c}{\partial \xi}\right)\right|_R \tag{9}$$

Let $P_{QV_c}^{-1} = [L_1 \quad L_2 \quad L_3 \quad L_4 \quad L_5]^T$. Equation (9) is left-multiplied by $L_i|_L$ $(i = 1, 2, \ldots, 5)$:

$$\begin{aligned} &\left[L_i JS_c - \left(\lambda_i \frac{\partial V_c}{\partial \xi}\right)\right]\Big|_L = L_i|_L \left[JS_c - \left(P_{QV_c}\Lambda \frac{\partial V_c}{\partial \xi}\right)\right]\Big|_R \\ &\rightarrow \left.\left(\lambda_i \frac{\partial V_c}{\partial \xi}\right)\right|_L = L_i|_L \left.\left(P_{QV_c}\Lambda \frac{\partial V_c}{\partial \xi}\right)\right|_R + L_i|_L[(JS_c)|_L - (JS_c)|_R] \end{aligned} \tag{10}$$

Similarly,

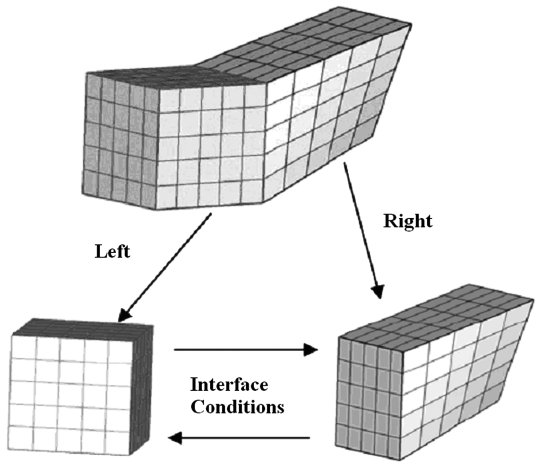


**Fig. 1 Two point-matched blocks with interface conditions.**

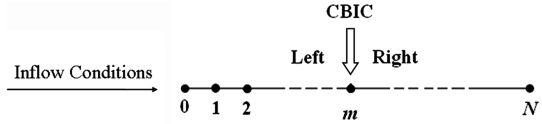


**Fig. 2 Sketch of the CBIC.**

$$\left.\left(\lambda_i \frac{\partial V_c}{\partial \xi}\right)\right|_R = L_i|_R \left.\left(P_{QV_c}\Lambda \frac{\partial V_c}{\partial \xi}\right)\right|_L + L_i|_R[(JS_c)|_R - (JS_c)|_L] \tag{11}$$

For the block on the left side of the interface, from Eq. (7), one can get

$$L_i|_L \left.\frac{\partial Q}{\partial t}\right|_L = \left.\left[JL_iS_c - L_i P_{QV_c}\Lambda \frac{\partial V_c}{\partial \xi}\right]\right|_L = \left.\left[JL_iS_c - \lambda_i \frac{\partial V_c}{\partial \xi}\right]\right|_L \tag{12}$$

Let a positive eigenvalue denote that the characteristic wave propagates from the left to the right. For positive eigenvalues,

$$L_i|_L \frac{\partial Q}{\partial t} = \frac{1 + \mathrm{sign}(\lambda_i)}{2} \left.\left[L_i JS_c - \lambda_i \frac{\partial V_c}{\partial \xi}\right]\right|_L \tag{13}$$

For negative eigenvalues,

$$L_i|_L \left.\frac{\partial Q}{\partial t}\right|_L = \frac{1 - \mathrm{sign}(\lambda_i)}{2} \left.\left[L_i JS_c - \lambda_i \frac{\partial V_c}{\partial \xi}\right]\right|_L \tag{14}$$

The negative eigenvalues indicate that the characteristic information shall be calculated in according to the right-hand flowfield of the interface. Substitute Eq. (10) into Eq. (14):

$$\begin{aligned} &L_i|_L \left.\frac{\partial Q}{\partial t}\right|_L = \frac{1 - \mathrm{sign}(\lambda_i)}{2}(L_i JS_c)|_L \\ &- \frac{1 - \mathrm{sign}(\lambda_i)}{2}\left[L_i|_L \left.\left(P_{QV_c}\Lambda \frac{\partial V_c}{\partial \xi}\right)\right|_R + L_i|_L[(JS_c)|_L - (JS_c)|_R]\right] \\ &\rightarrow L_i|_L \left.\frac{\partial Q}{\partial t}\right|_L = \frac{1 - \mathrm{sign}(\lambda_i)}{2} L_i|_L \left[(JS_c)|_R - \left.\left(P_{QV_c}\Lambda \frac{\partial V_c}{\partial \xi}\right)\right|_R\right] \end{aligned} \tag{15}$$

Combine Eq. (13) and (15) together:

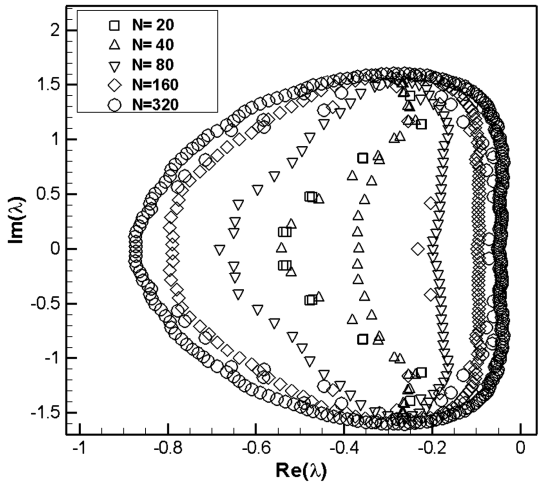


**Fig. 3 Eigenvalue spectra of the WCNS-E-5 with the CBIC, $m = N/2$.**

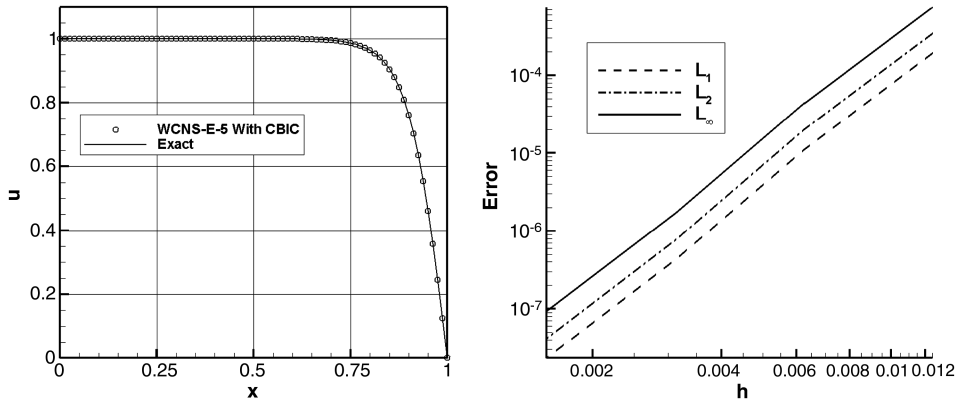


**a) Computed results** **b) Grid covergence**

**Fig. 4 Results for Eq. (34).**

$$
\begin{aligned}
&P_{QVc}^{-1}|_L \frac{\partial Q}{\partial t}\bigg|_L = \mathrm{diag}\left(\frac{1+\mathrm{sign}(\lambda_i)}{2}\right) P_{QVc}^{-1}|_L \left[JS_c - P_{QVc}\left|\left(\Lambda \frac{\partial V_c}{\partial \xi}\right)\right|\right]\bigg|_L \\
&+\mathrm{diag}\left(\frac{1-\mathrm{sign}(\lambda_i)}{2}\right) P_{QVc}^{-1}|_L \left[(JS_c)|_R - P_{QVc}|_R\left(\Lambda \frac{\partial V_c}{\partial \xi}\right)\right]_R|_L \\
&\rightarrow \frac{\partial Q}{\partial t}\bigg|_L = P_{QVc}|_L \mathrm{diag}\left(\frac{1+\mathrm{sign}(\lambda_i)}{2}\right) P_{QVc}^{-1}|_L \left[JS_c - P_{QVc}\Lambda \frac{\partial V_c}{\partial \xi}\right]\bigg|_L \\
&+P_{QVc}|_L \mathrm{diag}\left(\frac{1-\mathrm{sign}(\lambda_i)}{2}\right) P_{QVc}^{-1}|_L \left[JS_c - P_{QVc}\Lambda \frac{\partial V_c}{\partial \xi}\right]\bigg|_R
\end{aligned} \tag{16}
$$

Define

$$
\begin{aligned}
A_s^- &= P_{QVc}\mathrm{diag}\left(\frac{1-\mathrm{sign}(\lambda_i)}{2}\right) P_{QVc}^{-1} \\
A_s^+ &= P_{QVc}\mathrm{diag}\left(\frac{1+\mathrm{sign}(\lambda_i)}{2}\right) P_{QVc}^{-1}
\end{aligned} \tag{17}
$$

Then $A_s^+ + A_s^- = I$, and Eq. (16) can be expressed as

$$
\begin{aligned}
\frac{\partial Q}{\partial t}\bigg|_L &= (A_s^+)|_L \left[JS_c - P_{QVc}\Lambda \frac{\partial V_c}{\partial \xi}\right]\bigg|_L \\
&+ (A_s^-)|_L \left[JS_c - P_{QVc}\Lambda \frac{\partial V_c}{\partial \xi}\right]\bigg|_R
\end{aligned} \tag{18}
$$

From Eqs. (4) and (6), one can get

$$
\begin{aligned}
S_c - J^{-1}P_{QVc}\Lambda \frac{\partial V_c}{\partial \xi} &= -\left[F\frac{\partial J^{-1}\xi_x}{\partial \xi} + G\frac{\partial J^{-1}\xi_y}{\partial \xi}\right. \\
&\left. + H\frac{\partial J^{-1}\xi_z}{\partial \xi} + \frac{\partial J^{-1}\xi_t Q}{\partial \xi} + \frac{\partial \widehat{G}}{\partial \eta} + \frac{\partial \widehat{H}}{\partial \zeta}\right] \\
&- \left(J^{-1}\xi_x \frac{\partial F}{\partial \xi} + J^{-1}\xi_y \frac{\partial G}{\partial \xi} + J^{-1}\xi_z \frac{\partial H}{\partial \xi}\right) + s\cdot \mathrm{RHS}_V \\
&= -\left(\frac{\partial \widehat{F}}{\partial \xi} + \frac{\partial \widehat{G}}{\partial \eta} + \frac{\partial \widehat{H}}{\partial \zeta}\right) + s\cdot \mathrm{RHS}_V \\
&= \mathrm{RHS}_I + s\cdot \mathrm{RHS}_V
\end{aligned} \tag{19}
$$

Let

$$
\mathrm{RHS} = J\left(s\cdot \mathrm{RHS}_V + \mathrm{RHS}_I\right) \tag{20}
$$

Substituting Eqs. (19) and (20) into Eq. (18), one can get the following characteristic-based interface conditions (CBICs):

$$
\frac{\partial Q}{\partial t}\bigg|_L = \mathrm{RHS}^{\mathrm{new}} = (A_s^+)|_L(\mathrm{RHS})|_L + (A_s^-)|_L(\mathrm{RHS})|_R \tag{21}
$$

Similarly,

$$
\frac{\partial Q}{\partial t}\bigg|_R = \mathrm{RHS}^{\mathrm{new}} = (A_s^+)|_R(\mathrm{RHS})|_R + (A_s^-)|_R(\mathrm{RHS})|_L \tag{22}
$$

The interface conditions for the viscous terms are simple, as follows:

$$
\mathrm{RHS}_V^* = \tfrac{1}{2}(\mathrm{RHS}_V|_L + \mathrm{RHS}_V|_R) \tag{23}
$$

After applying Eq. (23), the algorithm for the viscous terms becomes symmetrical.

At the end, the time integration can be easily carried out for the points on the interface by the same producer as those for the inner points. The CBICs are more convenient to use than the original CIC/GCIC [21–23], as there is no longer a need to convert the governing equations to characteristic forms or to compute characteristic wave-amplitude vectors or other intermediate variables.

To eliminate numerical round-off errors, in addition to the CBIC, a simple averaging procedure is employed for the points on an interface:

$$
\frac{\partial Q^*}{\partial t} = \frac{1}{2}\left(\frac{\partial Q}{\partial t}\bigg|_L + \frac{\partial Q}{\partial t}\bigg|_R\right) \tag{24}
$$

$$
Q^* = \frac{(Q_L + Q_R)}{2} \tag{25}
$$

**Table 1 Accuracy order of WCNS-E-5 with CBIC for Burgers equation**

| Grid size | $L_1$ error | Accuracy order | $L_2$ error | Accuracy order | $L_\infty$ error | Accuracy order |
|---|---|---|---|---|---|---|
| 0.0125000 | 1.92E − 04 | —— | 3.45E − 04 | —— | 7.56E − 04 | —— |
| 0.0062500 | 1.11E − 05 | 4.11 | 2.00E − 05 | 4.11 | 4.42E − 05 | 4.09 |
| 0.0031250 | 4.29E − 07 | 4.69 | 7.75E − 07 | 4.69 | 1.71E − 06 | 4.69 |
| 0.0015625 | 2.32E − 08 | 4.21 | 4.19E − 08 | 4.21 | 9.28E − 08 | 4.21 |

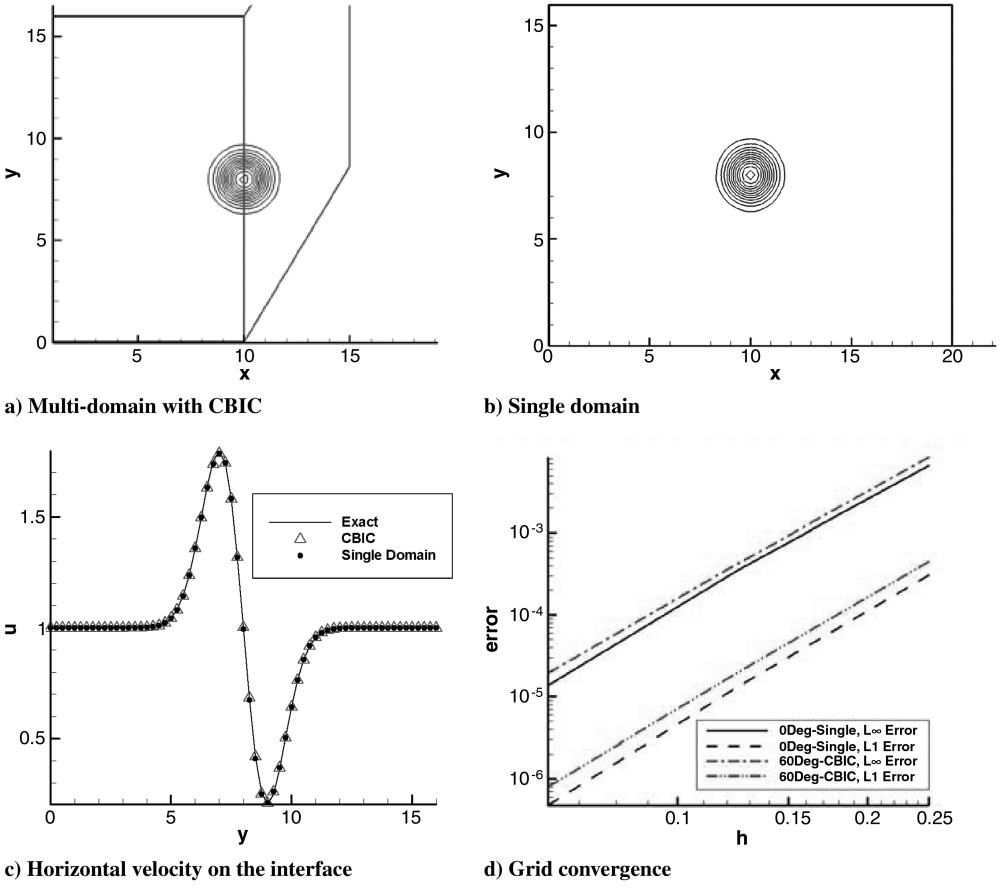


**Fig. 5 Performance of the CBIC on meshes with an abrupt change of slope at the interface.**

## III. Implementation of CBIC for WCNS-E-5 Scheme on Multiblock Grids

### A. WCNS-E-5 Scheme

The WCNS-E-5 scheme [9,10] is a formally fifth-order nonlinear scheme for inviscid terms. Let us first consider the discretization of the inviscid flux derivative along the $\xi$ direction. The discretization for other inviscid flux derivatives can be computed by similar procedures.

The WCNS-E-5 scheme can be expressed as

$$\frac{\partial \widehat{F}_i}{\partial \xi} = \frac{75}{64h}(\widehat{F}_{i+1/2} - \widehat{F}_{i-1/2}) - \frac{25}{384h}(\widehat{F}_{i+3/2} - \widehat{F}_{i-3/2}) + \frac{3}{640h}(\widehat{F}_{i+5/2} - \widehat{F}_{i-5/2}) \tag{26}$$

where $h$ is the grid size, and

$$\widehat{F}_{i+1/2} = \widehat{F}(U^L_{i+1/2}, U^R_{i+1/2}, \widehat{\xi}_{x,i+1/2}, \widehat{\xi}_{y,i+1/2}, \widehat{\xi}_{z,i+1/2}) \tag{27}$$

Here, Eq. (27) is computed by Steger–Warming flux-splitting method in the present work. WCNSs can be implemented on various types of variables [9], and $U$ are adopted here to denote conservative variables, primitive variables, or characteristic variables. In this paper, we chose primitive variables. Then $U^L_{i+1/2}$ and $U^R_{i+1/2}$ are the left and right primitive variables on cell edges. The high-order nonlinear weighted interpolation derived by Deng and Zhang [9] is applied here. The idea is that each of the chosen stencils is assigned a weight factor, which determines its contribution to the final approximation of the midnode value. The weights are designed in such a way that in the smooth region they approach the optimal weights to achieve fifth-order accuracy, whereas in the regions near the discontinuities, the weight of the stencil, which contains the discontinuities, is assigned nearly zero. Therefore, the weighted interpolations can prevent numerical oscillations around discontinuities.

Nonomura et al. [13] have given some detailed study on the freestream and vortex preservation properties of WCNS and WENO. It is worth noting that the main differences between WCNS and WENO are follows:

For WCNS, high-order nonlinear *interpolations* are adopted to get the cell-edge variables $U^{WCNS,L/R}_{j+1/2}$:

$$\begin{cases} U^{\mathrm{WCNS},L}_{i+1/2} = \mathcal{W}^{\mathrm{WCNS},L}(U_{i-r+1}, \ldots, U_{i+r}) + \mathcal{O}(h^{2r-1}) \\ U^{\mathrm{WCNS},R}_{i+1/2} = \mathcal{W}^{\mathrm{WCNS},R}(U_{i-r+2}, \ldots, U_{i+r}) + \mathcal{O}(h^{2r-1}) \\ \widehat{F}^{\mathrm{WCNS}}_{i+1/2} = \widehat{F}(U^{\mathrm{WCNS},L}_{i+1/2}, U^{\mathrm{WCNS},R}_{i+1/2}, \widehat{\xi}_{x,i+1/2}, \widehat{\xi}_{y,i+1/2}, \widehat{\xi}_{z,i+1/2}) \\ \kappa \frac{\partial \widehat{F}_{i-1}}{\partial \xi} + \frac{\partial \widehat{F}_i}{\partial \xi} + \kappa \frac{\partial \widehat{F}_{i+1}}{\partial \xi} = \frac{1}{h}\sum_k \alpha_k \widehat{F}^{\mathrm{WCNS}}_{i+1/2+k} \end{cases} \tag{28}$$

where $\mathcal{W}^{\mathrm{WCNS},L/R}$ denotes the weighted interpolating procedure, as presented in [9], and $\kappa$ and $\alpha_k$ are coefficients. When $\kappa = 0$,

**Table 2 Accuracy order of WCNS-E-5 with CBIC for skewed grids and smooth grids**

| | 60-deg-skewness multidomain with CBIC | | | | Single domain (without skewness) | | | |
|---|---|---|---|---|---|---|---|---|
| $h$ | $L_\infty$ | Accuracy order | $L_1$ | Accuracy order | $L_\infty$ | Accuracy order | $L_1$ | Accuracy order |
| 0.25 | 8.57E − 3 | —— | 4.50E − 4 | —— | 6.66E − 3 | —— | 3.07E − 4 | —— |
| 0.125 | 4.33E − 4 | 4.31 | 2.00E − 5 | 4.49 | 3.60E − 4 | 4.21 | 1.33E − 5 | 4.28 |
| 0.0625 | 1.93E − 5 | 4.49 | 7.93E − 7 | 4.66 | 1.38E − 5 | 4.70 | 4.74E − 7 | 4.79 |

$\alpha_0 = -\alpha_{-1} = 75/64, \quad \alpha_1 = -\alpha_{-2} = -25/384, \quad \alpha_2 = -\alpha_{-3} = 3/640$, and the last equation in Eq. (28) is equal to Eq. (26).

The nonlinear interpolations based on primitive variables are

$$U^L_{i+1/2} = U_i + \frac{1}{2}hf^*_{L\,i} + \frac{1}{8}h^2 s^*_{L\,i}$$

$$U^R_{i-1/2} = U_i - \frac{1}{2}hf^*_{R\,i} + \frac{1}{8}h^2 s^*_{R\,i} \qquad f^*_{L\,i} = \sum_{k=1}^{3}\omega_{L\,k} f^k_i$$

$$s^*_{L\,i} = \sum_{k=1}^{3}\omega_{L\,k} s^k_i \qquad f^*_{R\,i} = \sum_{k=1}^{3}\omega_{R\,k} f^k_i \qquad s^*_{R\,i} = \sum_{k=1}^{3}\omega_{R\,k} s^k_i$$

$$f^1_i = \frac{1}{2h}[U_{i-2} - 4U_{i-1} + 3U_i] \qquad s^1_i = \frac{1}{h^2}[U_{i-2} - 2U_{i-1} + U_i]$$

$$f^2_i = \frac{1}{2h}[(U)_{i+1} - (U)_{i-1}] \qquad s^2_i = \frac{1}{h^2}[U_{i-1} - 2U_i + U_{i+1}]$$

$$f^3_i = \frac{1}{2h}[-3U_i + 4U_{i+1} - U_{i+2}] \qquad s^3_i = \frac{1}{h^2}[U_i - 2U_{i+1} + U_{i+2}]$$

$$\omega_{L\,k} = \frac{\beta_{Lk}}{\sum_{m=1}^{3}\beta_{Lm}} \qquad \omega_{R\,k} = \frac{\beta_{Rk}}{\sum_{m=1}^{3}\beta_{Rm}} \qquad \beta_{Lk} = \frac{C_{Lk}}{(\varepsilon + IS_k)^2}$$

$$\beta_{Rk} = \frac{C_{Rk}}{(\varepsilon + IS_k)^2} \qquad IS_k = (hf^k_i)^2 + (h^2 s^k_i)^2$$

$$C_{L1} = C_{R3} = \frac{1}{16} \qquad C_{L2} = C_{R2} = \frac{10}{16} \qquad C_{L3} = C_{R1} = \frac{5}{16}$$

where $C_{L1} \sim C_{L3}$ and $C_{R1} \sim C_{R3}$ are the optimized coefficients to ensure fifth-order interpolations as follows:

$$\begin{cases} U^{L,\mathrm{op}}_{i+1/2} = \frac{1}{128}(3U_{i-2} - 20U_{i-1} + 90U_i + 60U_{i+1} - 5U_{i+2}) + \mathcal{O}(h^5) \\ U^{R,\mathrm{op}}_{i+1/2} = \frac{1}{128}(-5U_{i-1} + 60U_i + 90U_{i+1} - 20U_{i+2} + 3U_{i+3}) + \mathcal{O}(h^5) \end{cases} \tag{29}$$

For WENO, nonlinear *reconstructions* of fluxes are adopted to get $\widehat{F}^{\mathrm{WENO}}_{j+1/2}$:

$$\begin{cases} \widehat{F}^{\mathrm{WENO},+}_{i+1/2} = \mathcal{W}^{\mathrm{WENO},+}(\widehat{F}_{i-r+1}, \ldots, \widehat{F}_{i+r-1}) \\ \widehat{F}^{\mathrm{WENO},-}_{i+1/2} = \mathcal{W}^{\mathrm{WENO},-}(\widehat{F}_{i-r+2}, \ldots, \widehat{F}_{i+r}) \\ \widehat{F}^{\mathrm{WENO}}_{i+1/2} = \widehat{F}^{\mathrm{WENO},+}_{i+1/2} + \widehat{F}^{\mathrm{WENO},-}_{i+1/2} \\ \frac{\partial F^{\mathrm{WENO}}_i}{\partial \xi} = \frac{1}{h}(\widehat{F}^{\mathrm{WENO}}_{i+1/2} - \widehat{F}^{\mathrm{WENO}}_{i-1/2}) + \mathcal{O}(h^{2r-1}) \end{cases} \tag{30}$$

where $\mathcal{W}^{\mathrm{WENO},\pm}$ denotes the weighted reconstructing procedure, as presented in [29].

The procedures of the CBICs for WCNS-E-5 are as follows:

1) Get the RHS in each individual block. For example, the $\mathrm{RHS}_I$ in Eq. (20) can be calculated by WCNS-E-5. If the governing equations contain viscous terms, $\mathrm{RHS}_V$ are also computed, and Eq. (23) is applied to the $\mathrm{RHS}_V$ on interfaces.

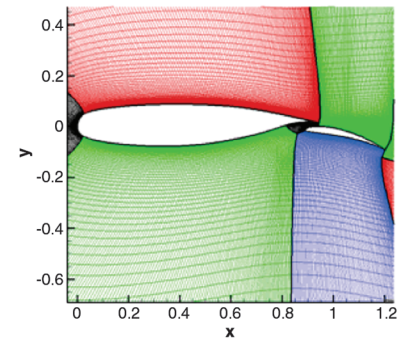


a) Grids

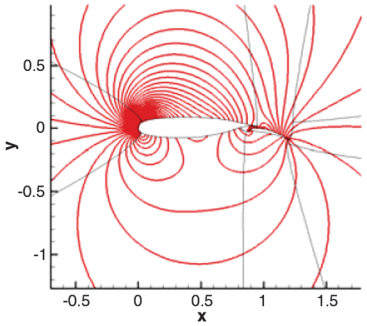


b) Pressure contours

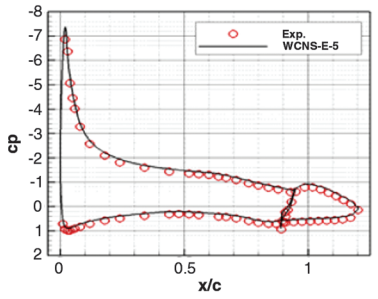


c) Pressure coefficient along chord distance

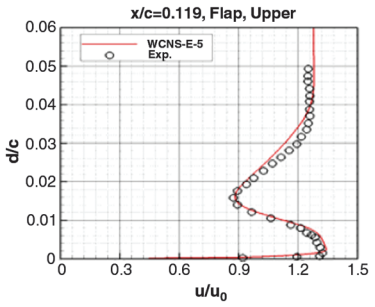


d) Velocity profiles at x/c = 0.119, flap

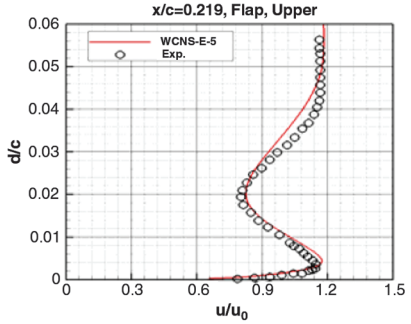


e) Velocity profiles at x/c = 0.219, flap

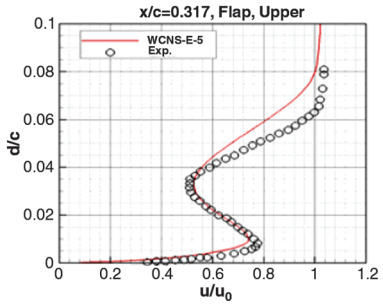


f) Velocity profiles at x/c = 0.317, flap

**Fig. 6 Grids and results of NLR7301 two-element airfoil.**

2) Modify the RHS of an interface by Eq. (21) for the left-hand-side block or by Eq. (22) for the right-hand-side block.

3) Eliminate round-off errors by Eq. (24).

4) Obtain $Q$ by a time-integration method such as the Runge–Kutta method.

5) If $Q$ belong to an interface, they are modified by Eq. (25) to eliminate round-off errors.

For the viscous terms, the fourth-order central explicit scheme [10] is adopted here, and the three-step Runge–Kutta method or the lower/upper symmetric Gauss–Seidel method is adopted for temporal integration. In addition, the geometric conservation law is very important for high-order difference schemes, even when the grid is stationary [12]. A conservation metric method that can ensure the discrete geometric conservation law for any high-order-accuracy schemes is given in [12]. This method is employed in this paper to compute the metrics such as $\widehat{\xi}_x$.

### B. Asymptotic Stability of the WCNS-E-5 Scheme with the CBIC

Consider the following linear hyperbolic system:

$$\frac{\partial u}{\partial t} + a\frac{\partial u}{\partial x} = 0 \tag{31}$$

where $a > 0$ is a constant speed. The domain is uniformity discretized into $N$ nodes with grid size $h$. Supposing that the field is decomposed into two parts at point $m$ (see Fig. 2), connecting by the CBIC, the semidiscretized form of Eq. (31) can be written as

$$\frac{\mathrm{d}\mathbf{u}}{\mathrm{d}t} = \frac{a}{h}\mathbf{D}\mathbf{u} + \mathbf{g}(t) \tag{32}$$

where $\mathbf{u} = [u_1, \ldots, u_m, u_{m+1}, \ldots, u_N]^T$, $\mathbf{g}(t)$ corresponds to the initial and boundary conditions (without losing generality, we set $\mathbf{g}(t) = 0$), and $\mathbf{D}$ is the difference matrix. Here, the CBICs are

$$\frac{\mathrm{d}u_m}{\mathrm{d}t} = \mathrm{RHS}_L = -c\frac{\partial u_m}{\partial x}|_L$$

The CBICs are contained in $\mathbf{D}$ at the connecting point $m$ as follows:

$$\mathbf{D} = \{d_{ij}\} = \begin{cases} d^L_{i,j} & \text{if } 1 \le i \le m \quad \text{and} \quad 1 \le j \le m \\ d^R_{i-m,j-m} & \text{if } m+1 \le i \le N \quad \text{and} \quad m \le j \le N \\ 0 & \text{else} \end{cases} \tag{33}$$

where $d^L_{i,j}$ and $d^R_{i,j}$ $(i = 1, 2, \ldots)$ are the components of $\mathbf{D}_L$ and $\mathbf{D}_R$, respectively. $\mathbf{D}_L = \mathbf{A}_L\mathbf{B}_L$, and $\mathbf{D}_R = \mathbf{A}_R\mathbf{B}_R$. Here, $\mathbf{A}_L$, $\mathbf{A}_R$, $\mathbf{B}_L$, and $\mathbf{B}_R$ are specified by the optimized WCNS-E-5 scheme and the boundary schemes. For example,

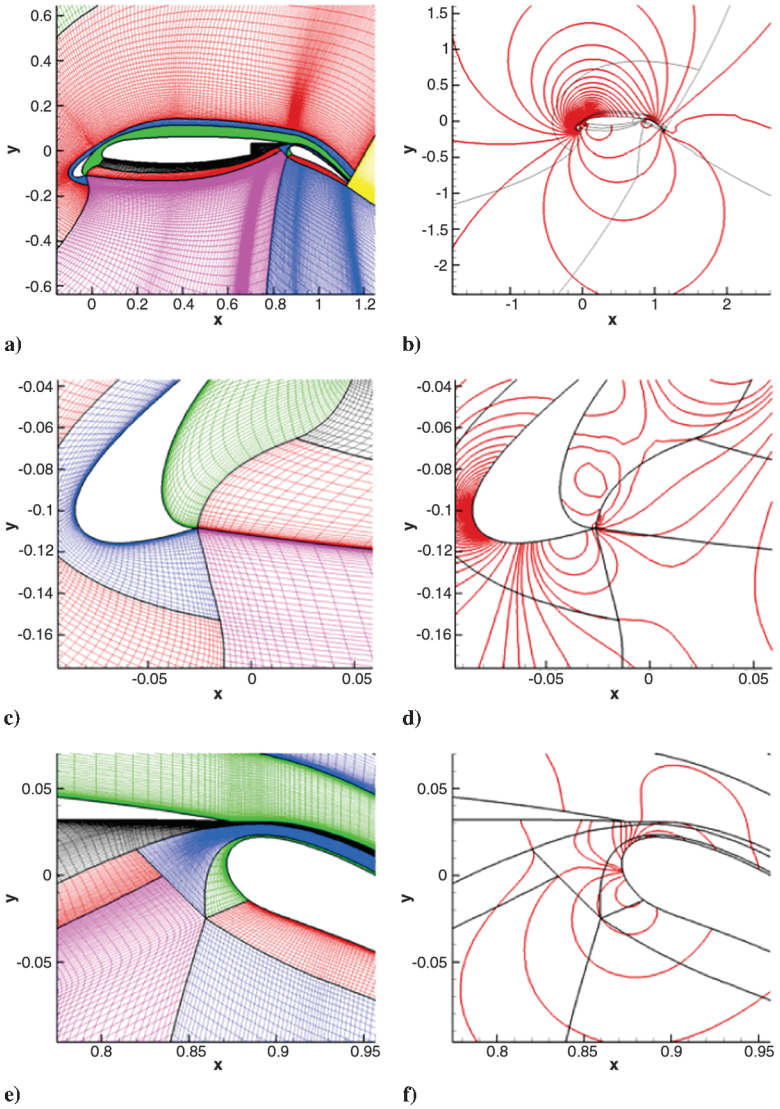


**Fig. 7 Grids and pressure contours of 30P-30N three-element airfoil.**

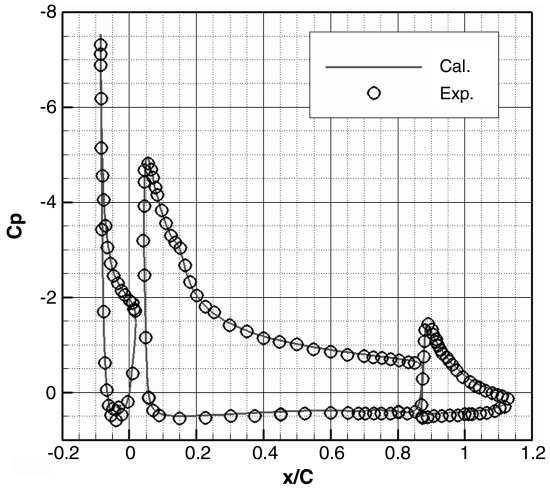


**Fig. 8 Wall pressure coefficient distributions.**

$L_2$, and $L_\infty$ errors and the corresponding orders of accuracy are shown in Table 1. It is obvious that the present method is fourth-order-accurate.

## IV. Applications and Discussions

To validate the CBIC and to show the potential ability of high-order scheme in solving engineering problems, the following two- and three-dimensional benchmark cases are simulated. These are a vortex convection problem, subsonic flows over NLR7301 two-element airfoil, subsonic flows over 30N-30P three-element airfoil, and transonic flows over DLR-F6.

### A. Vortex Convection Across an Interface

This case is chosen to validate the CBIC. The governing equations are the nondimensional Euler equations. The flow is set to be two-dimensional with $(u, v, p, T) = (1, 0, 1, 1)$. The initial condition is imposed by prescribing a vortex, centered at the location $(x_c, y_c)$, and satisfying the following relations:

$$\mathbf{A}_L = -\frac{1}{24}\begin{bmatrix} -23 & 21 & 3 & -1 & & & & & & \\ & -22 & 17 & 9 & -5 & 1 & & & & \\ & 1 & -27 & 27 & -1 & & & & & \\ & -\frac{9}{80} & \frac{25}{16} & -\frac{225}{8} & \frac{225}{8} & -\frac{25}{16} & \frac{9}{80} & & & \\ & & \ddots & \ddots & \ddots & \ddots & \ddots & \ddots & & \\ & & & -\frac{9}{80} & \frac{25}{16} & -\frac{225}{8} & \frac{225}{8} & -\frac{25}{16} & \frac{9}{80} & \\ & & & & & 1 & -27 & 27 & -1 & \\ & & & & -1 & 5 & -9 & -17 & 22 & \\ & & & & & & 1 & -3 & -21 & 23 \end{bmatrix}_{(0\sim m)\times(0\sim m+1)}$$

$$B_L = \frac{1}{16}\begin{bmatrix} 35 & -35 & 21 & -5 & & & & \\ 5 & 15 & -5 & 1 & & & & \\ -1 & 9 & 9 & -1 & & & & \\ \frac{3}{8} & -\frac{20}{8} & \frac{90}{8} & \frac{60}{8} & -\frac{5}{8} & & & \\ & \ddots & \ddots & \ddots & \ddots & \ddots & & \\ & & \frac{3}{8} & -\frac{20}{8} & \frac{90}{8} & \frac{60}{8} & -\frac{5}{8} & \\ & & & -1 & 9 & 9 & -1 & \\ & & & 1 & -5 & 15 & 5 & \\ & & & -5 & 21 & -35 & 35 \end{bmatrix}_{(0\sim m+1)\times(0\sim m)}$$

The asymptotic stability condition for the semidiscretized equation is that all eigenvalues of the matrix **D** have no positive real parts. Figure 3 shows the eigenvalue spectra of **D**. It can be seen that the WCNS-E-5 scheme with the CBIC is asymptotically stable.

### C. Accuracy Analysis in Solving the Burgers Equation

To show the accuracy of the present method for nonlinear viscous problems, the following Burgers equation is chosen as a model problem:

$$\frac{\partial u}{\partial t} + \frac{\partial f}{\partial x} = \mu \frac{\partial^2 u}{\partial x^2} \tag{34}$$

where $f = u^2/2$, $\mu = 0.05$, and $x \in [0, 1]$. The boundary conditions is $u(t, 0) = 1$ and $u(t, 1) = 0$. The analytical solution for this problem is

$$u(x) = \bar{u}\frac{1 - \exp[(x-1)\bar{u}/\mu]}{1 + \exp[(x-1)\bar{u}/\mu]}, \qquad \frac{\bar{u}-1}{\bar{u}+1} = \exp[-\bar{u}/\mu] \tag{35}$$

The computed domain is split into two sections. The left section is $x \in [0, 0.75]$, and the right section is $x \in [0.75, 1]$. The point at $x = 0.75$ is collected by the CBIC. Figure 4a shows the result of $h = 1/80$. The grid convergence result is shown in Fig. 4b. The $L_1$,

$$\begin{cases} \delta u = \frac{\varepsilon}{2\pi} e^{(1-r^2)/2}(y_c - y), & \delta v = \frac{\varepsilon}{2\pi} e^{(1-r^2)/2}(x - x_c) \\ \delta T = \frac{(\gamma-1)\varepsilon^2}{8\gamma\pi^2} e^{1-r^2}, & \delta S = 0 \\ r^2 = (x - x_c)^2 + (y - y_c)^2 \end{cases} \tag{36}$$

where $S$ is the entropy, and $e$ is the natural number. The computational domains are shown in Fig. 5a. An interface is imposed at $x = 10$ with an abrupt change of the slope on its two sides. The left-side domain is $x \in [0, 10]$ and $y \in [0, 16]$ with the $41 \times 65$ orthogonal mesh, while the right-side domain is 60 deg away from orthogonality with $41 \times 65$ points.

Starting from $t = 0$ with initial position $x_c = 5$ and $y_c = 8$, the computation is carried out until the vortex core arrived at the interface ($t = 5$). Figures 5a and 5b show the pressure contours of the multidomain field and a single-domain field, respectively. The single domain is a uniform $81 \times 65$ grid without the interface or the abrupt change of slope. The distribution of $u$ along the interface is shown in Fig. 5c. It is obvious that, due to the effectiveness of the CBIC, excellent agreement between the result computed on the skewed grid and the result computed on the single domain is obtained, and both results are very close to the theoretical distribution. The grid convergence for $L_\infty$ errors and $L_1$ errors of $\rho$ are shown in Fig. 5d. The errors as well as the order of accuracy are listed in Table 2. Because one-side schemes are necessary for the RHS of the interface,

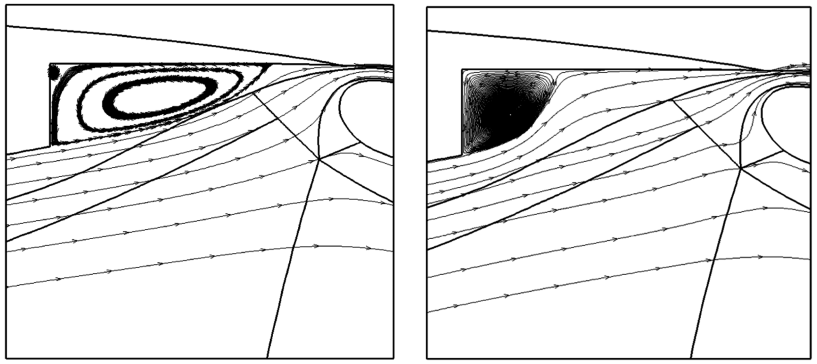

a) WCNS-E-5 b) NND (secnod order)

**Fig. 9 Streamlines.**

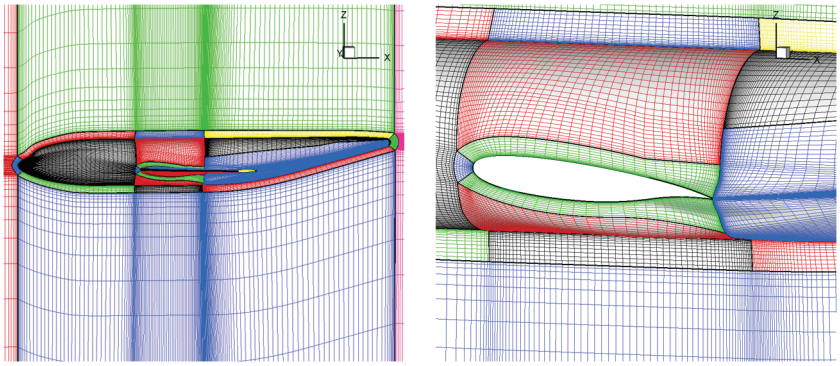

**Fig. 10 Grids for the wing-body configuration.**

the errors of the multiblock grids (with an abrupt skewness) are greater than that of the single-block grids (without skewness). However, it can be found that the CBIC can preserve the formal accuracy of WCNS-E-5.

### B. NLR7301 Two-Element Airfoil

The Reynolds-averaged Navier–Stokes equations are used as the governing equations. The Spalart–Allmaras one-equation turbulence model [30] is applied hereafter without the trip function of $f_{t1}$ and $f_{t2}$. In this paper, the turbulence model is discretized by the second-order nonoscillatory and non-free-parameter dissipative (NND) scheme [31] for simplicity.

Comprehensive experimental results about the airfoil can be found in [32]. Case 2 of [32] is chosen in this paper. The incoming flow conditions are as follows. Mach number is 0.185, Reynolds number is $2.51 \times 10^6$, angle of attack is 6.0 deg, flap deflection angle is 20.0 deg, gap width is 1.3%, and overlap width is 5.3%.

The grid system is shown in Fig. 6a, and the computed pressure contours are shown in Fig. 6b. It can be seen that the result is very smooth without any spurious oscillations, despite there being many interfaces. Figure 6c shows the pressure coefficient along the nondimensional chord distance. Good agreement between the WCNS-E-5 result and the experimental result is acquired. Figures 6d–6f show the boundary velocity profiles at three different chord locations, where $c$ denotes the chord length of the main foil or the flap, and $x$ denotes the chord distance between a measured position and the forefront point of an element foil. Figures 6d–6f indicate qualitative agreements between the WCNS-E-5 results and the experimental results. The experimental lift coefficient and drag coefficient are 2.366 and 0.0225, respectively. The computed results are 2.461 and 0.0276, correspondingly. The difference between the experimental results and the computational results is about 4% for lift coefficient and 23% for drag coefficient. The main purpose of this paper is to introduce the CBIC as well as to show the ability of the WCNS-E-5 in solving complex configuration problems. The discrepancies between the numerical results and the experimental results indicate that, in addition to high-order schemes, many other aspects such as far-field boundary, wall boundary, Euler flux, and transition still remain to affect the accuracy of CFD.

### C. 30P-30N Three-Element Airfoil

This is a classic case to check the stability of a scheme, because the flow is complex with many shear layers. The flow is supposed to be full turbulence, and the inflow conditions are $Ma = 0.2$, $Re = 9 \times 10^6$, and $T_\infty = 300$ K.

Figure 7 contains the grids and pressure contours. Some enlarged parts near the complex connecting points are also shown in Figs. 7c–7f. For quantitative validation of the accuracy of the present high-order strategy, the pressure coefficient distributions on the wall are given in Fig. 8. The computational results are in good agreement with the experimental results. The streamlines near the main foil tail are shown in Fig. 9: Fig. 9a shows WCNS-E-5, and Fig. 9b shows the second-order NND scheme [31]. The WCNS-E-5 scheme successfully resolves the small secondary vortex in the corner of the main foil, while the second-order scheme fails.

### D. DLR-F6 with FX2B Wing-Body Fairing

From 2001 to 2009, the AIAA Applied Aerodynamics Technical Committee sponsored four Drag Prediction Workshops (DPW), with the aim of assessing the state-of-the-art current CFD solvers at predicting absolute and incremental drag changes on generic transonic transport aircraft configurations.**

We conduct the present study in according to DPW-III. The DLR-F6 wing-body configuration with the FX2B fairing is chosen to show the potential applications of the WCNS-E-5 scheme for general aircraft configurations. The flow conditions are $Ma = 0.75$,

**Data available online at http://aaac.larc.nasa.gov/tsab/cfdlarc/aiaa-dpw [retrieved 20 September 2010].

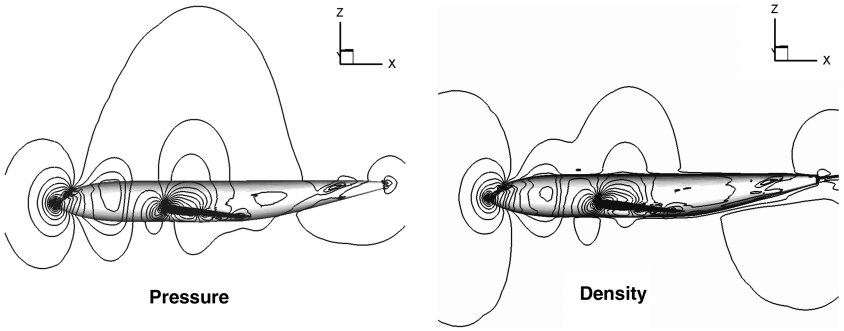


Fig. 11 Pressure and density contours ($\alpha = 0°$).

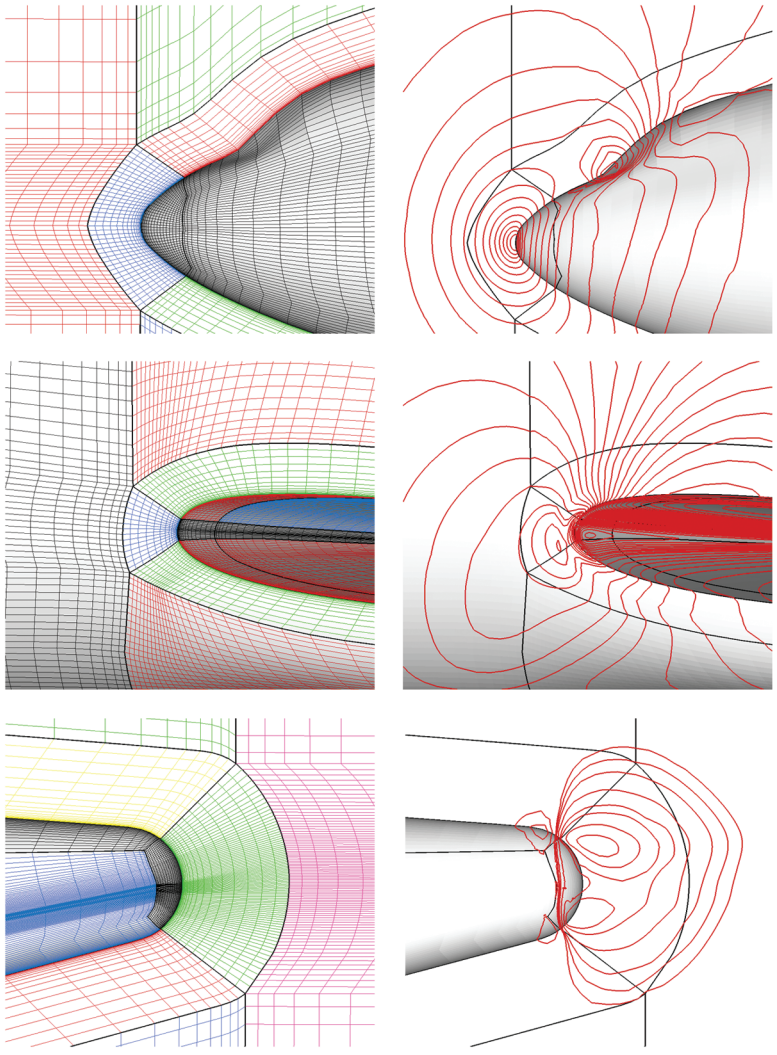

Fig. 12 Grids and pressure contours at the nose (top), the wing-body junction (middle), and the tail (bottom). $\alpha = 0°$.

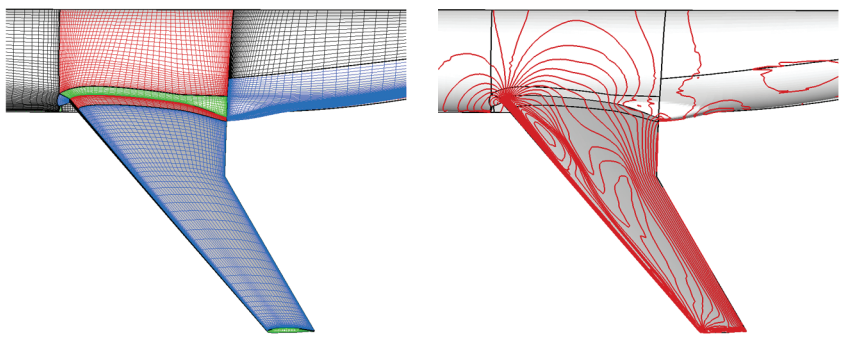

Fig. 13 Grids and pressure contours on the leeward of the wing ($\alpha = 0°$).

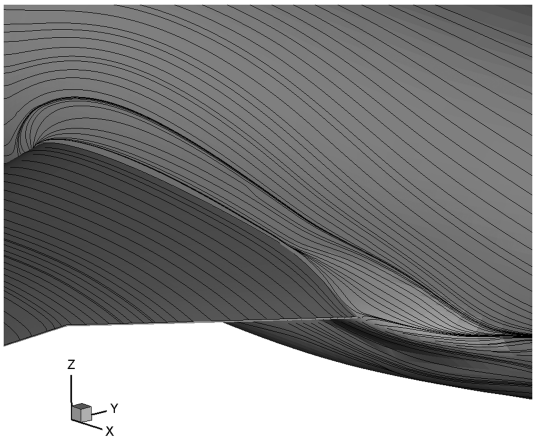


**Fig. 14 Surface streamlines near the wing-body junction ($\alpha = 0°$).**

$Re = 5 \times 10^6$, $T_\infty = 322.22$ K, and $\alpha = 0°$. The reference quantities are half-model reference area $S/2 = 72,700$ mm$^2$, mean aerodynamic chord $c_{\text{ref}} = 141.22$ mm, projected half-span $b/2 = 585.647$ mm, and aspect ratio AR $= 9.5$

The grid number is 4.28 million, which is a coarse one when compared with the grids of DPW-III. The grid system is shown in Fig. 10. The computed pressure contours and density contours are shown in Fig. 11. The close-up views near the nose, the wing-body junction, and the tail, where the grid topology is complex, are shown in Fig. 12. The surface grids and pressure contours of the wing are shown in Fig. 13. The surface streamlines are shown in Fig. 14. When $\alpha = 0°$, the computed lift coefficient is 0.4763, and drag coefficient is 0.0294. When $C_l = 0.5$, we get $C_d = 0.0304$.

## V. Conclusions

WCNSs are a kind of high-order nonlinear scheme and have been used for a large range of flow simulations. We successfully applied the fifth-order WCNS (WCNS-E-5) to complex grid systems. The characteristic-based interface conditions (CBIC), which are very convenient for practical applications, are proposed in order to fulfill the high-order schemes on complex grids. With the CBIC, a high-order strategy for complex point-matched multiblock grids is presented. The high-order WCNS-E-5 scheme with the CBIC was proven to be asymptotically stable in linear system with uniform grids. Validation of the CBIC with WCNS-E-5 is given by solving the Burgers equation and a vortex convection problem. Numerical results show that the CBIC can keep the high-order accuracy of WCNS-E-5. For two- and three-dimensional engineering-oriented problems, the strategy performs excellently, despite the grids being very complex with multiple connecting points. Further investigations will be carried on in the aspects such as wall boundary treatments and transition, which may degrade the performance of the high-order WCNS processes for engineering-oriented applications.

## Acknowledgments

This study was supported by the project of National Natural Science Foundation of China (grant nos. 10621062 and 11072259) and National Basic Research Program of China (grant no. 2009CB723800). The authors would like to thank Laiping Zhang, Shuhai Zhang, Guangxue Wang, Xin Liu, and Junwu Hong for their contributions and useful suggestions.

## References

[1] Wang, Z. J., "High-Order Methods for The Euler and Navier–Stokes Equations on Unstructured Grids," *Progress in Aerospace Sciences*, Vol. 43, 2007, pp. 1–41. doi:10.1016/j.paerosci.2007.05.001

[2] Ekaterinaris, J. A., "High-Order Accurate, Low Numerical Diffusion Methods for Aerodynamics," *Progress in Aerospace Sciences*, Vol. 41, 2005, pp. 192–300. doi:10.1016/j.paerosci.2005.03.003

[3] Lele, S. K., "Compact Finite Difference Schemes with Spectral-Like Resolution," *Journal of Computational Physics*, Vol. 103, 1992, pp. 16–42. doi:10.1016/0021-9991(92)90324-R

[4] Deng, X., Maekawa, H., and Shen, Q., "A Class of High Order Dissipative Compact Schemes," AIAA Paper 96-1972, 1996.

[5] Visbal, M. R., and Gaitonde, D. V., "High-Order Accurate Methods for Complex Unsteady Subsonic Flows," *AIAA Journal*, Vol. 37, No. 10, 1999, pp. 1231–1239. doi:10.2514/2.591

[6] Tu, G-H., Yuan. X- J., Xia, Z-Q, and Hu, Z., "A Class of Compact Upwind TVD Difference Schemes," *Journal of Applied Mathematics and Mechanics*, Vol. 27, No. 6, 2006, pp. 765–772. doi:10.1007/s10483-006-0607-1

[7] Tu, G-H., and Yuan, X-J., "A Characteristic-Based Shock-Capturing Scheme for Hyperbolic Problems," *Journal of Computational Physics*, Vol. 225, 2007, pp. 2083–2097. doi:10.1016/j.jcp.2007.03.007

[8] Deng, X., and Maekawa, H., "Compact High-Order Accurate Nonlinear Schemes," *Journal of Computational Physics*, Vol. 130, 1997, pp. 77–91. doi:10.1006/jcph.1996.5553

[9] Deng, X., and Zhang, H., "Developing High-Order Accurate Nonlinear Schemes," *Journal of Computational Physics*, Vol. 165, 2000, pp. 22–44. doi:10.1006/jcph.2000.6594

[10] Deng, X., "High-Order Accurate Dissipative Weighted Compact Nonlinear Schemes," *Science in China, Series A (Mathematics, Physics, Astronomy and Technological Sciences)*, Vol. 45, No. 3, 2002, pp. 356–370. doi:10.1360/02ys9037

[11] Liu, X., Deng, X., and Mao, M. L., "High-Order Behaviors of Weighted Compact Fifth-Order Nonlinear Schemes," *AIAA Journal*, Vol. 45, No. 8, 2007, pp. 2093–2097. doi:10.2514/1.23797

[12] Deng, X., Mao, M., Tu, G., Zhang, Y., and Zhang, H., "High-Order and High-Accurate CFD Methods and Their Applications," 8th Asian Computational Fluid Dynamics Conference, Hong Kong, Paper ACFD0126-T002-A-001, 10–14 Jan. 2010.

[13] Nonomura, T., Iizuka, N., and Fujii, K., "Freestream and Vortex Preservation Properties of High-Order WENO and WCNS on Curvilinear Grids," *Computers and Fluids*, Vol. 39, 2010, pp. 197–214. doi:10.1016/j.compfluid.2009.08.005

[14] Sumi, T., Kurotaki, T., and Hiyama, J., "Generalized Characteristic Interface Conditions with High-Order Interpolation Method," AIAA Paper 2008-752, 2008.

[15] Gaitonde, D. V., and Visbal, M. R., "Padé-Type High-Order Boundary Filters for the Navier–Stokes Equations," *AIAA Journal*, Vol. 38, No. 11, 2000, pp. 2103–2112. doi:10.2514/2.872

[16] Delfs, J. W., "Sound Generation From Gust-Airfoil Interaction Using CAA-Chimera Method," AIAA Paper 2001-2136, 2001.

[17] Sherer, S. E., Gordnier, R. E., and Visbal, M. R., "Computational Study of a UCAV Configuration Using a High-Order Overset-Grid Algorithm," AIAA Paper 2008-626, 2008.

[18] Sherer, S. E., and Scott, J. N., "High-Order Finite-Difference Methods on General Overset Grids," *Journal of Computational Physics*, Vol. 210, 2005, pp. 459–496. doi:10.1016/j.jcp.2005.04.017

[19] Rai, M. M., "A Relaxation Approach to Patched Grid Calculations with the Euler Equations," *Journal of Computational Physics*, Vol. 66, 1986, pp. 99–131. doi:10.1016/0021-9991(86)90056-2

[20] Lerat, A., and Wu, Z. N., "Stable Conservative Multidomain Treatments for Implicit Euler Equations," *Journal of Computational Physics*, Vol. 123, 1996, pp. 45–64. doi:10.1006/jcph.1996.0004

[21] Kim, J. W., and Lee, D. J., "Characteristic Interface Conditions for Multi-Block High-Order Computation on Singular Structured Grid," AIAA Paper 2003-3122, 2003.

[22] Sumi, T., Kurotaki, T., and Hiyama, J., "Generalized Characteristic Interface Conditions for Accurate Multi-Block Computation," AIAA Paper 2006-1272, 2006.

[23] Sumi, T., Kurotaki. T., and Hiyama, J., "Practical Multi-Block Computation with Generalized Characteristic Interface Conditions Around Complex Geometry," AIAA Paper 2007-4471, 2007.

[24] Barth, T. J., "Aspects of Unstructured Grids and Finite-Volume Solvers

for the Euler and Navier-Stokes Equations," VKI Lecture Series 1994-05, von Karman Inst. for Fluid Dynamics, Rhode-Saint-Genèse, Belgium, 1995.

[25] Thompson, K. W., "Time Dependent Boundary Conditions for Hypersonic System, II," *Journal of Computational Physics*, Vol. 89, 1990, pp. 439–461. doi:10.1016/0021-9991(90)90152-Q

[26] Poinsot, T. J., and Lele, S. K., "Boundary Conditions for Direction Simulations of Compressible Viscous Flows," *Journal of Computational Physics*, Vol. 101, 1992, pp. 104–129. doi:10.1016/0021-9991(92)90046-2

[27] Okong'o, N., and Bellan, J., "Consistent Boundary Conditions for Multicomponent Real Gas Mixtures Based on Characteristic Waves," *Journal of Computational Physics*, Vol. 176, 2002, pp. 330–344. doi:10.1006/jcph.2002.6990

[28] Kim, J. W., and Lee, D. J., "Generalized Characteristic Boundary Conditions for Computational Aeroacoustics, Part 2," *AIAA Journal*, Vol. 42, No. 1, 2004, pp. 47–55. doi:10.2514/1.9029

[29] Jiang, G.-S., and Shu, C.-W., "Efficient Implementation of Weighted ENO Schemes," *Journal of Computational Physics*, Vol. 126, 1996, pp. 202–228. doi:10.1006/jcph.1996.0130

[30] Spalart, P. R., and Allmaras, S. R., "A One-Equation Turbulence Model for Aerodynamic Flows," AIAA Paper 92-0439, 1992.

[31] Zhang, H., and Zhuang, F., "NND Schemes and Their Applications to Numerical Simulation of Two- and Three-Dimensional Flows," *Advances in Applied Mechanics*, Vol. 29, 1991, pp. 193–256. doi:10.1016/S0065-2156(08)70165-0

[32] Van den, B., and Oskam, B., "Boundary Layer Measurements on a Two-Dimensional Wing with Flap and a Comparison with Calculations," National Aerospace Laboratory/NLR, TR 79009U, Emmeloord, The Netherlands, 1979.

W. Anderson
*Associate Editor*